Applied Catalysis B: Environmental 245 (2019) 1–9

Contents lists available at ScienceDirect

Applied Catalysis B: Environmental

journal homepage: www.elsevier.com/locate/apcatb

Epitaxial growth of oriented prussian blue analogue derived well-aligned $CoFe_2O_4$ thin film for efficient oxygen evolution reaction

Song Lei, Qiao-Hong Li, Yao Kang, Zhi-Gang Gu*, Jian Zhang*

State Key Laboratory of Structural Chemistry, Fujian Institute of Research on the Structure of Matter, Chinese Academy of Sciences, 350002 Fuzhou, PR China

ARTICLE INFO

Keywords:
Prussian blue analogous
Liquid phase epitaxial growth
$CoFe_2O_4$ thin film
Oxygen evolution reaction

ABSTRACT

The development of cost-effective, high-efficiency, and non-noble metal based electrocatalysts for oxygen evolution reaction (OER) is considered to be the most pivotal portion for electrochemical water splitting to generate renewable energy. Herein, well-aligned mesoporous $CoFe_2O_4$ thin film is first developed from surface epitaxial growth of oriented CoFe-based prussian blue analogue thin film (CoFe-PBA thin film) for efficient electrocatalytic OER. CoFe-PBA thin film with preferred [100] orientation is first prepared on the substrate surface by employing liquid phase epitaxial method without any structure-directing surfactants. After thermal pyrolysis, such CoFe-PBA thin film was transformed into well-aligned mesoporous $CoFe_2O_4$ thin film. Interestingly, the self-support $CoFe_2O_4$ thin film electrode with the mass loading of 1.6 mg cm^{-2} delivers an oxygen evolution current density of 10 mA cm^{-2} at an overpotential of 266 mV and exhibits durable stability in 1 M KOH aqueous solution. The remarkable and stable catalytic performance of the $CoFe_2O_4$ thin film can be mainly owing to the mesoporous structure of $CoFe_2O_4$, efficient charge/electron transfer, the numerous exposed active sites, and the well-structured configuration of the electrode. Hence, this work provides an effective paradigm for preparing binder-free, self-support, and low-cost spinel oxide electrocatalyst for efficient OER derived from surface epitaxial growth of oriented PBA thin film.

1. Introduction

Increasing consumption of fossil fuels has resulted in a series of global energy and environment issues. Water splitting driven by electricity energy is one of the most optimal strategies to produce renewable energy {Zheng, 2016 #269} [1–3]. However, as one of the half reaction of water splitting, oxygen evolution reaction (OER) is kinetically sluggish owing to the multistep proton-coupled electron transfer, which requires an efficient catalyst to promote the oxidation reaction kinetics [4–6]. Although RuO_2 and IrO_2 are currently regarded as the efficient OER catalysts, these precious metal-based catalysts with prohibitive costs and low abundance seriously prohibit their large-scale commercial applications [7,8]. Recently, transition-metal based bimetallic spinel oxides (AB_2O_4, A, B are metal elements) have emerged as significant candidates for the water oxidation catalysts due to their earth-abundant, inexpensive, low toxicity, and thermodynamic stability [9,10]. Notably, in the structure of AB_2O_4, B^{3+} and A^{2+} occupy all or part of the octahedral and tetrahedral sites, respectively [11], and the solid-state redox couples A^{3+}/A^{2+} and B^{3+}/B^{2+} easily occur, which offers a necessary surface redox active metal centers for the adsorption and activation of electroactive species [12,13].

Prussian blue analogues (PBA), a kind of significant coordination polymers [14], containing rich and tunable metal ions have been extensively studied for many applications like magnetics [15], batteries [16,17], supercapacitor [18,19], and catalysis [20,21]. Noticeably, PBA derived spinel oxides have been widely used in energy storage and conversion technologies like OER [22,23]. However, these electrocatalysts usually are powder materials, which requires drop-casting onto the current collector (glassy carbon electrode, Ni foam, carbon paper, and so on) with the assistance of polymeric binder. The working electrode prepared by this drop-casting method usually has mechanical brittleness and obvious interfacial gap, and the introduction of binders may cover up active sites, these critical problems seriously limits the OER application in water splitting [24]. Recently, metal–organic frameworks (MOFs) anchored on various substrates derived nano-catalysts like nanotubes, nanorods, and nanosheets has been demonstrated that they can effectively prevent catalyst aggregation and shedding [25–27]. Such nanostructured catalysts can expose more active sites and reduce the resistance of charge transfer, which is beneficial to improve electrochemical performance. However, up to now, there are few reports on the applications of PBA thin film derived catalysts for water oxidation, and the development of oriented PBA thin film is still a challenge but

* Corresponding author.
E-mail addresses: zggu@fjirsm.ac.cn (Z.-G. Gu), zhj@fjirsm.ac.cn (J. Zhang).

https://doi.org/10.1016/j.apcatb.2018.12.036
Received 23 August 2018; Received in revised form 9 December 2018; Accepted 14 December 2018
Available online 15 December 2018
0926-3373/

important in the electrochemical application. On the other hand, in the synthesis of powder PBA, chelating agent sodium citrate or surfactant PVP is usually used to control the crystallization process and prevent the aggregation of nanoparticles [16,28,29], which is not economical and environmentally friendly.

In the last few years, liquid phase epitaxial (LPE) method for preparation of MOFs on various substrates indicates some advantages like high orientation, tunable thickness, and compact film [30,31]. During the LPE process, the two MOF precursor solutions (e.g., metal ions and organic ligand solutions) are separated and the functionalized substrate is alternately immersed into two precursor solutions with layer-by-layer procedure for some time. The samples are rinsed with solvent for removing the residual precursor between each step. Finally, the repeated growth cycles are used for the fabrication of MOF thin film on the substrate surface. Such surface-mounted MOFs thin film (SURMOFs) have been used widely in a number of potential applications, such as adsorption/separation [32,33], catalysis [34,35], biocompatibility [36], devices [37,38], and sensors [39,40]. These results inspire us to explore a new strategy to prepare PBA film derived electrocatalyst for improving their catalytic performance. Herein, we first use a facile LPE layer-by-layer strategy for preparing oriented CoFe-based PBA thin film (CoFe-PBA thin film) without structure-directing surfactant. Subsequently, the same strategy was adopted to prepare CoFe-PBA thin film on a 3D conductive Ni foam substrate. After calcining in air, such oriented CoFe-PBA thin film was transformed into well-aligned mesoporous $CoFe_2O_4$ thin film, and the catalyst loading can be adjusted by controlling the number of LPE cycles in the synthesis of CoFe-PBA thin film. Noticeably, $CoFe_2O_4$ thin film with the mass loading of 1.6 mg cm^{-2} was used as the working electrode exhibits efficient OER catalytic activity and outstanding stability in alkaline electrolyte.

2. Experimental

2.1. Materials and instrumentation

All the reagents and solvents employed were commercially available and were used as received without further purification. Ni foam and Cu foam were purchased from Hefei Kejing Material Technology Co., Ltd. Powder X-ray diffraction (PXRD) analysis was performed on a MiniFlex2 X-ray diffractometer using Cu-Kα radiation (λ = 0.1542 nm). Transmission electron microscope (TEM) specimens were prepared by sonication the as-prepared samples from Ni foam substrate, followed by dispersing them in ethanol and collecting them on the TEM copper grids. TEM images were obtained in JEM-2010 F. Scanning electron microscope (SEM) images and elements mapping were measured by JSM6700. X-ray photoelectron spectroscopy (XPS) spectra for the samples were measured by ESCALAB250Xi. The BET was measured at liquid nitrogen (77 K) by ASAP 2010 analyzer. Temperature programmed reduction (TPR) was conducted with a mixture of 5% H_2/Ar (50 mL min^{-1}) and the temperature was increased from 50 °C to 800 °C at a heating rate 10 °C min^{-1} by AutoChem II 2920. The contact angle was measured by Contact Angle Meter JC2000D1 employing a sessile drop method. Electrochemical measurements were carried out by Zahner-Zennium IM6 and the CHI760E electrochemical workstation (CH Instrument, Inc.).

2.1.1. Preparation of CoFe-based prussian blue analogue thin film on Si substrate

CoFe-based prussian blue analogue thin film (CoFe-PBA thin film) was grown on Si substrate through the liquid-phase epitaxy (LPE) approach with an automatic pump system under 60 ℃ water bath conditions. A piece of Si (1 cm × 3 cm) was pre-treated with base piranha solution. Followed by rinsing with ethanol and deionized water, respectively, and dried under nitrogen flux for the next sample preparation. The cleaned Si substrate was immersed into a 1 mM aqueous solution of $Co(OAc)_2{\cdot}4H_2O$ for 30 min and subsequently into a 2 mM aqueous solution of $K_3[Fe(CN)_6]$ for 30 min at 60 °C. The samples were rinsed with deionized water for 60 s between each step. A total of 10 growth cycles were used for the fabrication of CoFe-PBA thin film on Si substrate.

2.1.2. Preparation of CoFe-based prussian blue analogue thin film on Ni foam and Cu foam substrate

CoFe-based prussian blue analogue thin film (CoFe-PBA thin film) was grown on Ni foam surface through the LPE approach with an automatic pump system under 60 °C water bath conditions. A piece of Ni foam (1 cm × 3 cm, thickness: 1 mm) was pre-treated with HCl solution (3 M) and base piranha solution. Followed by sonication in ethanol and deionized water for 10 min, respectively, and drying in air for next sample preparation. The cleaned Ni foam was immersed into a 1 mM aqueous solution of $Co(OAc)_2{\cdot}4H_2O$ for 30 min and subsequently into a 2 mM aqueous solution of $K_3[Fe(CN)_6]$ for 30 min at 60 °C. The samples were rinsed with deionized water for 60 s between each step. A total of 10 growth cycles were used for the fabrication of CoFe-PBA thin film on Ni foam. CoFe-PBA thin film was grown on Cu foam surface by the same procedure using Cu foam (1 cm × 3 cm, thickness: 1 mm) in place of Ni foam.

2.1.3. Preparation of $CoFe_2O_4$ thin film

The as-prepared CoFe-PBA thin film on Ni foam and Cu foam substrate were annealed at 350 °C for 120 min with a heating temperature rate of 5 ℃ min^{-1} in air. After cooling to room temperature, the $CoFe_2O_4$ thin film was obtained. The mass loading of the $CoFe_2O_4$ thin film on Ni foam was determined by inductively coupled plasma spectrometer (ICP). For comparison, bare Ni foam was annealed under the same conditions.

2.1.4. Fabrication of $CoFe_2O_4$ powder and commercial RuO_2 on Ni foam

$CoFe_2O_4$ powder was prepared by peeling off $CoFe_2O_4$ thin film from the Ni foam by sonication in ethanol for 30 min. Then, 2 mg of $CoFe_2O_4$ powder, 500 μL of ethanol and 25 μL of 5 wt% Nafion solution were mixed under 30 min sonication to form a homogeneous suspension solution. Afterwards, the catalyst suspension solution was recoated on the Ni foam (mass loading is ~1.6 mg cm^{-2}) using a drop-casting method. After the solvent evaporates at room temperature, $CoFe_2O_4$ powders loaded electrode was prepared. The commercial RuO_2 loaded electrode was prepared by the same procedure using 2 mg RuO_2 in place of $CoFe_2O_4$ powders.

2.2. Electrochemical measurements

All electrochemical measurements were conducted in CHI 760E electrochemical workstation (CH Instrument, Inc.) and Zahner-Zennium IM6 at room temperature (25℃) in a conventional three-electrode system using electrocatalysts loaded electrode as the working electrode (0.5 cm × 1 cm immersed in the electrolyte), Ag/AgCl (3 M KCl) and Pt wire were used as the reference electrode and the counter electrode. All tests were performed in 1 M KOH aqueous electrolyte. Prior to recording the linear sweep voltammetry (LSV) curves, several cyclic voltammetry (CV) cycles at a sweep rate of 100 mV s^{-1} were taken to stabilize their OER properties. LSV curves were recorded at a scan rate of 2 mV s^{-1} with iR-compensation by Rs. Electrochemical impedance spectroscopy (EIS) measurements were conducted in a frequency range from 0.1 Hz to 100 kHz with an amplitude of 5 mV. All potentials in present work were calibrated to reversible hydrogen electrode (RHE) according to the Nernst equation: E(RHE) = 0.197 V + 0.059 × pH + E(measured). And the presented current density was normalized to the geometric surface area (1 cm^2).

2.3. Turnover frequency (TOF) calculations

The TOF values were calculated according to the equation [24]:

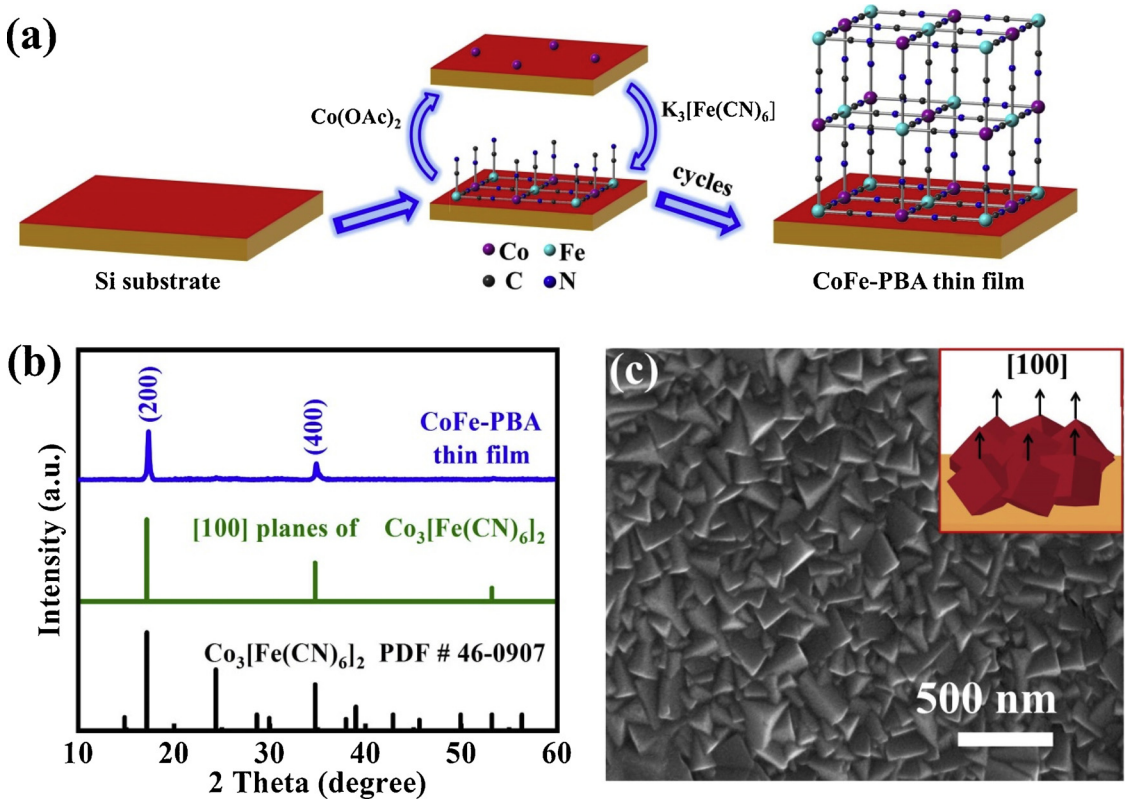

Fig. 1. (a) Schematic presentation of layer-by-layer growth of oriented CoFe-PBA thin film using liquid phase epitaxy (LPE) approach on Si substrate; (b) XRD and (c) SEM image (insert is the microstructure of the [100]-oriented CoFe-PBA) of CoFe-PBA thin film on Si substrate.

TOF = jA / 4Fn, where *j* is the current density at the given overpotential; A is the geometric surface area of electrode; 4 expresses the mole of electrons consumed for evolving one mole of oxygen from water; F is the faraday constant (96,485 C mol^{-1}); and *n* is molar number of catalyst, n = m/M (m is the mass loading of the catalyst on Ni foam substrate, M is the molecular weight of the catalyst unified with one active center per formula unit).

2.4. DFT calculations

The electronic structures of all catalysts were computed by Vienna Ab-initio Simulation Package (VASP). All calculations were performed with PBE exchange-correlation functional (the 1996 functional of Perdew, Burke, and Ernzerhof) on periodically repeated slabs [41]. All periodic slabs had a vacuum spacing of at least 15 Å. The structural model of $CoFe_2O_4$ contained six layers (including 24 Fe atoms, 12 Co atoms and 48 O atoms), with a = 8.381, b = 11.852, c = 22.486, α = β = γ = 90°. The top-view models were shown in Figure S19. In calculations, the three bottom layers were kept fixed, whereas the rest of atoms were allowed to relax. All structures were fully relaxed to the ground state. The convergence of energy and forces were set to 1×10^{-5} eV and 0.05 eV, respectively. An energy cutoff of 400 eV and a Gamma k-point sampling were found to get convergent geometry. An effective U parameter of 4.0 eV and spin were applied for Co/Fe 3d states to describe well the electronic structure of $CoFe_2O_4$ models.

2.5. Micro kinetic analysis

The micro kinetic process of water-splitting reaction is modeled with the approach used by Norskov and coworkers [42–44], which has been recently applied to two dimensional phosphorus porous polymorphs [45], graphitic carbon nitride supported single-atom catalysts [46], and arbon nitride monolayer [47]. Two half-reaction equations, i.e. OER and HER, are listed as below:

$$2H_2O \rightarrow O_2 + 4H^+ + 4e^- \quad (1)$$

$$4H^+ + 4e^- \rightarrow H_2 \quad (2)$$

For OER, Eq. (1) is decomposed into four one-electron steps OER-1 to OER-4 with each step generates one H^+ and an electron, listed as below:

$$* + H_2O\ (l) \rightarrow OH^* + (H^+ + 4e^-)\ \text{(OER-1)}$$

$$OH^* \rightarrow O^* + (H^+ + 4e^-)\ \text{(OER-2)}$$

$$O^* + H_2O(l) \rightarrow OOH^* + (H^+ + 4e^-)\ \text{(OER-3)}$$

$$OOH^* \rightarrow * + O_2\ (g) + (H^+ + 4e^-)\ \text{(OER-4)}$$

The Gibbs free energy change (ΔG_i) of each reaction step can be described as

$$\Delta G_i = \Delta E_i + \Delta ZPE_i + T\Delta S_i + \Delta G_u + \Delta G_{pH},$$

Where ΔE_i represents the DFT calculated reaction energy, ΔZPE_i refers to zero point energy change, T is the temperature, ΔS_i is entropy change, ΔG_u = -eU (U, the potential of the photogenerated electrons/holes with respect to the normal hydrogen electrode (NHE)), and $\Delta G_{pH} = \Delta G_{pH} = 2.303 k_B T \times$ pH. (k_B, the Boltzmann constant) The entropies of the free molecules can be taken from the NIST database (http://cccbdb.nist.gov/) and the energy contribution from the configuration entropy in the adsorbed state is not included. As a generally-accepted OER activity descriptor, the overpotential (η) for a chemical reaction can be calculated as follow:

$\eta = \max[\Delta G_1, \Delta G_2, \Delta G_3, \Delta G_4]/e - 1.23[v]$ (G_1, G_2, G_3, G_4 are the Gibbs free energy change of the OER-1, 2, 3, 4, respectively.)

This is independent of pH, and therefore applicable to water-alkali conditions.

3. Results and discussion

3.1. Preparation and characterization

The preparation of oriented CoFe-PBA thin film is shown in Fig. 1a. Briefly, CoFe-PBA was LPE layer-by-layer grown on Si substrate surface by immersing the dilute solution of $Co(OAc)_2{\cdot}4H_2O$ and $K_3[Fe(CN)_6]$ sequentially. After the growth of 10 LPE cycles, the oriented and homogeneous CoFe-PBA thin film can be well prepared on the flat substrate, which can be demonstrated by XRD patterns and SEM image. Fig. 1b exhibited he XRD patterns of the CoFe-PBA thin film on flat substrate. The diffraction peaks at 17.8° and 34.8° matched well with the (200) and (400) facets of $Co_3[Fe(CN)_6]_2$ (JCPDS No. 46-0907), which suggests the mainly preferred [100] crystal orientation for CoFe-PBA thin film. Scanning electron microscope (SEM) image of the oriented CoFe-PBA thin film (Fig. 1c) indicated that the surface of Si substrate was covered by a layer of interconnected CoFe-PBA with mainly exposed [100] crystal orientation. The successful preparation of CoFe-PBA thin film on flat Si substrate by LPE method indicated that this method can be extended to other substrates to prepare oriented PBA. Because Ni foam possesses rich 3D macroporous structure, high surface area, and superior conductivity, which can provide an ideal substrate for electrocatalytic reactions, the same strategy was adopted to prepare CoFe-PBA thin film on the Ni foam substrate (Fig. 2a). After thermal treatment, the color of the CoFe-PBA thin film changed from mauve to black (Figure S1), suggesting the formation of $CoFe_2O_4$ thin film, which can be demonstrated by XRD patterns in Fig. 3a. The mass loading of $CoFe_2O_4$ thin film on Ni foam is approximately 1.6 mg cm^{-2}, and the Fe/Co atomic ratio in $CoFe_2O_4$ thin film is about 2, which was determined by inductively coupled plasma spectrometer (ICP). Furthermore, the mass loading of electrocatalyst can be adjusted by controlling the number of LPE cycles in the synthesis of CoFe-PBA thin film. For instance, when the number of LPE cycles is 5 and 15 times, the mass loading of $CoFe_2O_4$ thin film on Ni foam is approximately 1.1 mg cm^{-2} and 2.4 mg cm^{-2}, respectively (Table S1).

The morphologies of CoFe-PBA thin film and $CoFe_2O_4$ thin film on Ni foam were investigated by SEM and transmission electron microscopy (TEM) in Figure 2b ~ j. After 10 LPE cycles, CoFe-PBA thin film was mounted at the Ni foam surface. The SEM images of CoFe-PBA thin film (Figure 2b ~ d) shown that uniform and oriented CoFe-PBA thin film was grown on the surface of Ni foam. The SEM images of bare Ni foam were also shown in Figure S2. After calcination in air at 350 °C, uniformly arranged Co and Fe metal atoms connected by organic ligand (-CN) in CoFe-PBA thin film are oxidized in situ into metal oxide

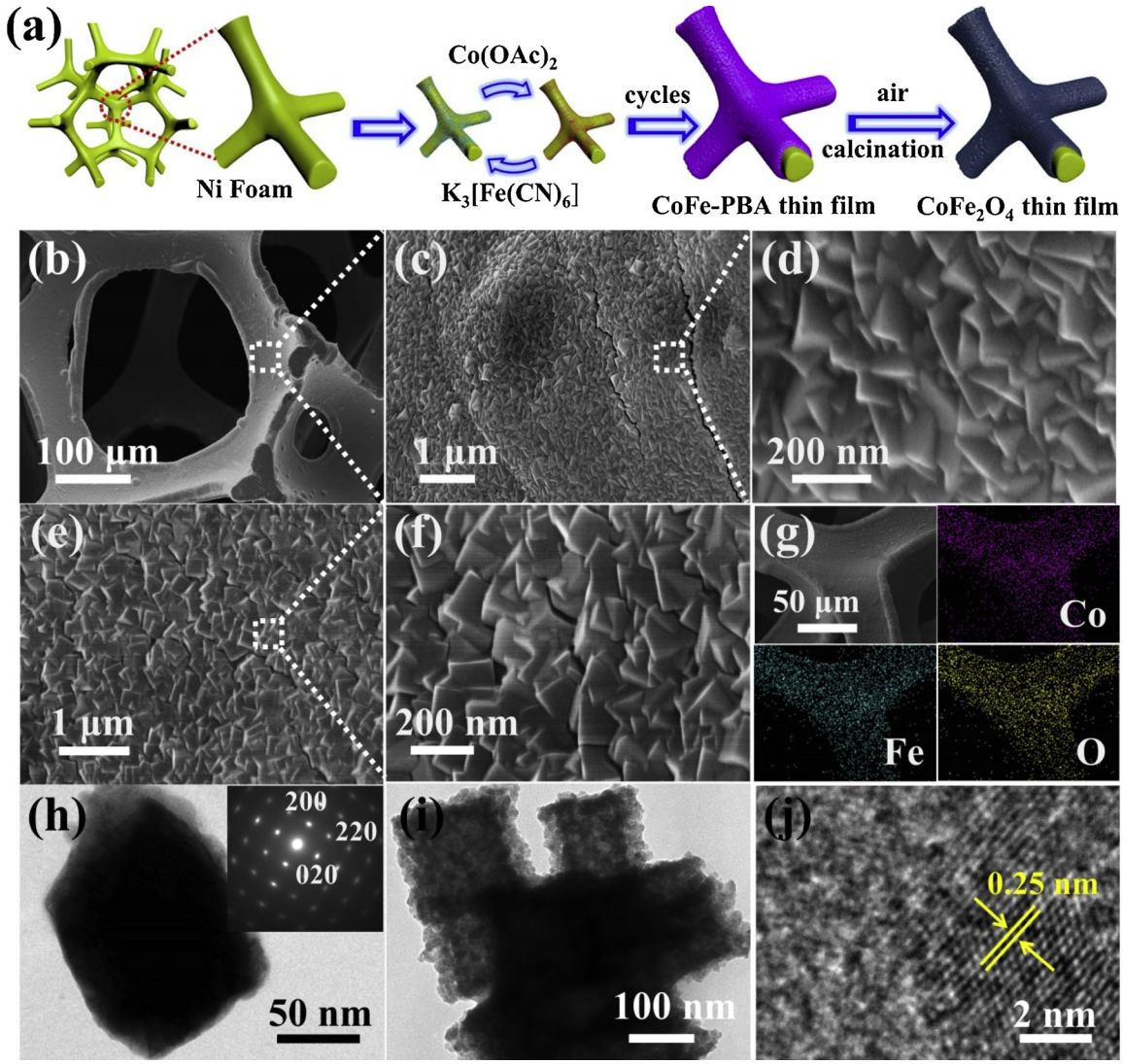

Fig. 2. (a) Schematic illustration of the formation of $CoFe_2O_4$ thin film on Ni foam; SEM images of (b ~ d) CoFe-PBA thin film and (e ~ f) $CoFe_2O_4$ thin film; (g) SEM-EDS elemental mapping of Co, Fe, and O in $CoFe_2O_4$ thin film; (h) TEM image of CoFe-PBA thin film (insert is the corresponding SAED); (i) TEM and (*j*) HRTEM images of $CoFe_2O_4$ thin film.

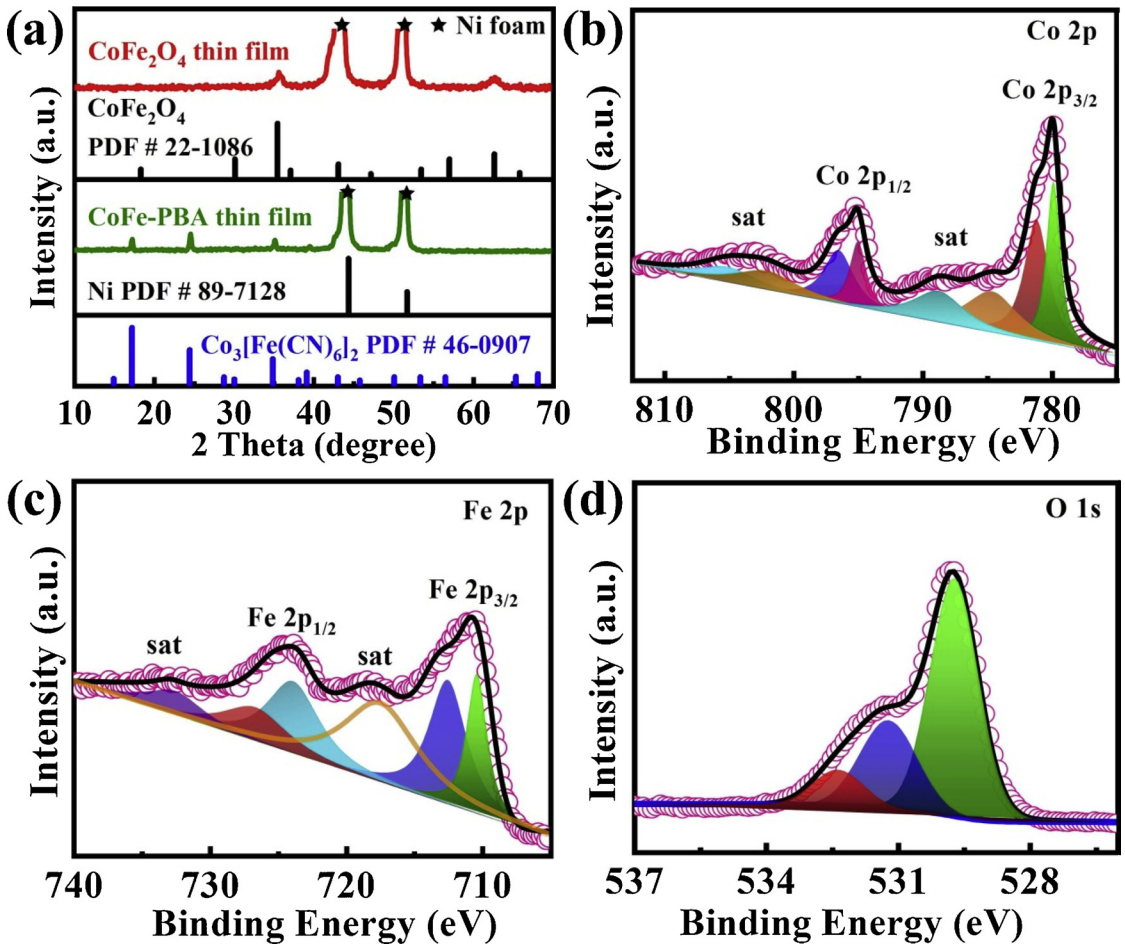

Fig. 3. (a) XRD patterns of CoFe-PBA thin film and $CoFe_2O_4$ thin film with decreased Y scale; XPS spectra of (b) Co 2p, (c) Fe 2p, and (d) O 1 s spectra in $CoFe_2O_4$ thin film (Sat means satellites).

nanoparticles, resulting $CoFe_2O_4$ thin film. The organic ligand (-CN) gradually decomposed and produced CO_2 and NO_x, which can effectively prevent the aggregation of nanoparticles and lead to numerous disordered pores inside $CoFe_2O_4$ thin film, thus maintaining a good morphology after calcination [48,49], as shown in the SEM images of $CoFe_2O_4$ thin film (Figure 2e∼f). The SEM-EDS elemental mapping of $CoFe_2O_4$ thin film (Fig. 2g) indicated the homogeneous distribution of Co, Fe, and O elements in the $CoFe_2O_4$ thin film. TEM image with selective area electron diffraction (SAED) pattern (Fig. 2h) indicated the successful formation of CoFe-PBA thin film with high crystallinity. TEM image of $CoFe_2O_4$ thin film (Fig. 2i) suggested that the collapse of -CN in CoFe-PBA thin film after pyrolysis, resulting $CoFe_2O_4$ thin film with unconsolidated structure. The high-resolution TEM image (HRTEM) for $CoFe_2O_4$ thin film (Fig. 2j) revealed that the lattice spacing with a distance of 0.25 nm corresponded well to the [311] planes of $CoFe_2O_4$ (JCPDS No. 22-1086). The high-angle annular dark field (HAADF) image and scanning transmission electron microscopes energy dispersive X-ray spectroscopy (STEM-EDX) elemental mapping images shown that Co, Fe, and O elements are uniformly distributed in $CoFe_2O_4$ thin film (Figure S3). Therefore, the $CoFe_2O_4$ thin film with well-aligned spatial form, compact film, and homogeneous surface was prepared on Ni foam surface successfully.

Fig. 3a displayed the XRD patterns of CoFe-PBA thin film and $CoFe_2O_4$ thin film on the Ni foam substrate. The diffraction peaks of CoFe-PBA thin film at 17.5°, 24.6°, 35.1°, and 39.5° matched well with the (200), (220), (400), and (420) peaks of $Co_3[Fe(CN)_6]_2$ (JCPDS No. 46-0907), respectively. The XRD patterns of the $CoFe_2O_4$ thin film shown diffraction peaks at 36.5° and 64.2° corresponding to (311) and (440) peaks of the $CoFe_2O_4$ (JCPDS No. 22-1086), respectively. Besides, the two strong peaks at 44.3° and 51.6° (marked by pentacle in Fig. 3a) are attributed to Ni foam substrate (JCPDS No. 89-7128). Brunauer-Emmett-Teller (BET) surface area of $CoFe_2O_4$ stripped from Ni foam was measured to be 34.4 $cm^{-2}\,g^{-1}$, and the pore size distribution indicated the mesoporosity of their internal structure (Figure S4). These mesoporous channels can facilitated the diffusion of electrolyte and the release of O_2 bubbles, which is favorable for the mass transfer to the accessible catalytic active sites [50]. Temperature-programmed reduction (TPR) profile of $CoFe_2O_4$ (Figure S5) displayed the characteristic peaks for the reduction of CoO to metallic cobalt couple with Fe_2O_3 to Fe_3O_4 at 416 °C, and the reduction of Fe_3O_4 to FeO and metallic Fe at 453 °C [51]. The wettability of CoFe-PBA thin film and $CoFe_2O_4$ thin film was also analyzed employing a sessile drop method. As exhibited in Figure S6, the contact angle (θ) of CoFe-PBA thin film and $CoFe_2O_4$ thin film were 48° and 16°, respectively. As expected, the $CoFe_2O_4$ thin film displayed the smaller contact angle, indicating an extremely hydrophilic surface. Such feature can effectively promote the diffusion of gases and facilitate the contact between electrode surface and electrolyte, which provides an opportunity to enhance the electrocatalytic OER performance [52].

X-ray photoelectron spectroscopy (XPS) survey spectrum of $CoFe_2O_4$ thin film (Figure S7) confirmed the existence of Co, Fe, and O. The high-resolution Co 2p profile (Fig. 3b) was well fitted into eight contributions, including two pairs of spin-orbit doublets and their shakeup satellites, indicating the existence of Co^{2+} and Co^{3+} in $CoFe_2O_4$ thin film [49]. For the Fe 2p XPS spectrum (Fig. 3c), the peaks at 710.2 and 723.9 eV were ascribed to Fe^{2+}, whereas the peaks at

712.6 eV and 725.6 eV and two satellite peaks at 718.5 eV and 732.7 eV were assigned to Fe^{3+} [53]. The O 1 s spectra (Fig. 3d) were deconvolved into three peaks. The peak at 529.8 eV is the typical metal-oxygen bonds, the peak at 531.4 eV is assigned to the defects with low oxygen in the surface of $CoFe_2O_4$ thin film, and the peak at 532.2 eV corresponds to the water molecules adsorbed at the surface [54]. These analysis results indicated the formation of $CoFe_2O_4$ thin film on Ni foam with rich surface redox active metal centers.

3.2. Electrochemical OER activity

3.2.1. OER performance: the role of $CoFe_2O_4$ thin film

Since the well-aligned mesoporous $CoFe_2O_4$ thin film with abundant surface redox active metal centers was anchored on the surface of 3D conductive Ni foam surface without any auxiliary adhesive, which may offer a good candidate for electrocatalytic OER. With the intention of getting insight into the well-aligned spatial form of $CoFe_2O_4$ thin film and the integrated electrode configuration on the electrocatalytic OER performance, $CoFe_2O_4$ powder were obtained by peeling off the $CoFe_2O_4$ thin film from the Ni foam substrate under ultrasound conditions, then recoated on the Ni foam with the same mass loading (1.6 mg cm^{-2}) by the assistance of auxiliary adhesive 5 wt% Nafion solution.

In order to compare the OER performance of the $CoFe_2O_4$ thin film, $CoFe_2O_4$ powder, commercial RuO_2, CoFe-PBA thin film, and Ni foam-350, a standard three-electrode cell in 1 M KOH was applied using a Pt wire electrode and a Ag/AgCl as the counter and reference electrodes, respectively. As depicted in Fig. 4(a ~ b) and Figure S8, the Ni foam-350 and CoFe-PBA thin film shown a very large OER overpotential of 442 mV and 378 mV at a geometric current density of 10 mA cm^{-2}. Noticeably, the $CoFe_2O_4$ thin film exhibited the highest electrocatalytic OER activity and can give rise to a geometric current density of 10 mA cm^{-2} at an overpotential of 266 mV, which is 45 mV and 65 mV lower than that of commercial RuO_2 benchmark and $CoFe_2O_4$ powder under the identical conditions. On the other hand, the present $CoFe_2O_4$ thin film also exhibited the smallest onset potential of 1.46 V versus RHE, estimated from the potential where the plot starts to deviate from the linear region as revealed by the arrow in Figure S9. Moreover, the overpotential at a geometric current density of 10 mA cm^{-2} for the $CoFe_2O_4$ thin film is the smallest among the previously reported transition metal powder oxides derived from powder PBA, such as Ni–Co-mixed oxide (380 mV) [23], Ni–Fe oxide (303 mV) [48], Ni_xFe_{3-x} (402 mV) [55], and much better or comparable than other transition metal oxide based electrocatalyst, the detailed comparison information was summarized in Table S2. The catalytic activity of $CoFe_2O_4$ thin film on Cu foam was also investigated under the same conditions (Figure S10). The overpotential (266 mV) of $CoFe_2O_4$ thin film on Ni foam is much lower than that (294 mV) of $CoFe_2O_4$ thin film on Cu foam, demonstrating the synergism effect between catalyst and Ni foam substrate for enhancing the OER catalytic activity. As shown in Fig. 4c, the Tafel slope of the $CoFe_2O_4$ thin film is about 53 mV dec^{-1}, which is lower than that of RuO_2 (58 mV dec^{-1}), $CoFe_2O_4$ powder (78 mV dec^{-1}), CoFe-PBA thin film (99 mV dec^{-1}), and Ni foam-350 (119 mV dec^{-1}). These results strongly indicated that the $CoFe_2O_4$ thin film activates water-oxidation reaction kinetics under alkaline conditions. It demonstrated that surface directly epitaxial growth of oriented PBA thin film derived electrocatalyst on Ni foam substrate can significantly improve OER performance.

3.2.2. The charge-transfer kinetics analysis

Electrochemical impedance spectrum (EIS) measurements were conducted from 0.1 Hz to 100 kHz to explore the electrode kinetics. As depicted in Fig. 4d inset, the semicircular diameter for $CoFe_2O_4$ thin film gradually decreased when the applied potential increased from 1.50 V to 1.53 V versus RHE, indicating a rather low charge-transfer resistance. The equivalent circuit simulated by EIS spectrum at 1.50 V versus RHE (Fig. 4d) is revealed in Figure S11, it can be seen that the electrolyte resistance (Rs) of both $CoFe_2O_4$ thin film and $CoFe_2O_4$ powder are 1.61 Ω. The charge transfer resistance (Rct) of $CoFe_2O_4$ thin film and $CoFe_2O_4$ powder is 5.28 and 10.72 Ω, respectively. The smaller Rct of $CoFe_2O_4$ thin film mainly attribute to the internal mesoporous structure of $CoFe_2O_4$ and further tightly bonding with 3D conductive mesoporous Ni foam, which can be demonstrated by the cross-section SEM image of $CoFe_2O_4$ thin film (Figure S12). It clearly shown that $CoFe_2O_4$ thin film with the thickness of approximately 200 nm is tightly attached to the Ni foam substrate, which can effectively promote the transfer of charge/electron (Fig. 4a inset displayed the model of electron/charge transfer at the interface of electrolyte and electrodes), offer a faster OER kinetics, and significantly enhance the OER performance [56]. In the $CoFe_2O_4$ powder loaded working electrode, the well-aligned spatial form of $CoFe_2O_4$ thin film was totally or partially destroyed by ultrasound (Figure S13). In addition, the $CoFe_2O_4$ powder were recoated on the substrate by mechanical drop-casting method, leading to observably increase the pathway of electron/charge transfer and resistance at the interface of electrolyte and electrodes, which may be responsible for the OER performance of $CoFe_2O_4$ powder degradation compared with the initial $CoFe_2O_4$ thin film.

3.2.3. Intrinsic OER activity comparison

The electrocatalytic active surface areas (ECSA) of the catalyst was estimated from the double layer capacitance (C_{dl}), which was calculated by employing a simple cyclic voltammetry (CV) method [57]. As shown in Figure S14, the C_{dl} of $CoFe_2O_4$ thin film and $CoFe_2O_4$ powder is 10.9 and 5.2 m F cm^{-2}, respectively. The C_{dl} can be further converted to ECSA according to the previous reports [58]. The ECSA of the $CoFe_2O_4$ thin film and $CoFe_2O_4$ powder were calculated to be 7.8 and 3.7 cm^2_{ECSA}, respectively. The larger ECSA can offer more accessible catalytic active sites for adsorption of OH^- [59], thus expediting oxygen evolution during the oxidation–reduction reaction in water splitting. After the well-organized structure of $CoFe_2O_4$ thin film was destroyed, its ECSA is significantly reduced, which mainly due to the partial active sites were covered by the adhesive and the aggregation of the powder catalyst. For compare the intrinsic activity of the $CoFe_2O_4$ thin film and $CoFe_2O_4$ powder, the geometric current densities were further normalized to ECSA. As shown in Fig. 3d, the $CoFe_2O_4$ thin film can offer a normalized current density of 10 mA cm^{-2} at an overpotential of 290 mV, which is 60 mV lower than that of $CoFe_2O_4$ powder. The TOFs of the $CoFe_2O_4$ thin film, $CoFe_2O_4$ powder, and RuO_2 are 0.0698, 0.0053 and 0.0037 s^{-1} at the overpotential of 330 mV, the largest TOF of the $CoFe_2O_4$ thin film indicates its highest catalytic property for OER, compared with $CoFe_2O_4$ powder and RuO_2. This is also corresponding to the lowest Tafel slope and the overpotential at the same current density in $CoFe_2O_4$ thin film. These results fully illustrated that the self-support $CoFe_2O_4$ thin film with well-aligned spatial form conducive to expose more catalytic active sites, resulting in the enhancement of OER performance.

3.2.4. Stability test

The long-time durability of the electrocatalyst is another pivotal parameter for its further practical applications in energy conversion system. In this work, chronoamperometric was employed to test the stability of the electrocatalyst in 1 M KOH. As shown in Figs. 4f and S15, after 24 h of OER reaction with a current density of ~20 mA cm^{-2}, the anode current density of $CoFe_2O_4$ thin film shown almost no obvious attenuation, and the corresponding LSV curve exhibited slight attenuation, suggesting superior stability of the $CoFe_2O_4$ thin film electrode in 1 M KOH. In contrary, $CoFe_2O_4$ powder and RuO_2 loaded electrodes eventually exhibited 13.5% and 14.8% attenuation compared to the initial current density, which may be attribute to the aggregation or shedding of the catalyst in the process of continuous oxygen production. Furthermore, the long-term stability of $CoFe_2O_4$ thin film at high current density was explored in 1 M KOH. As depicted

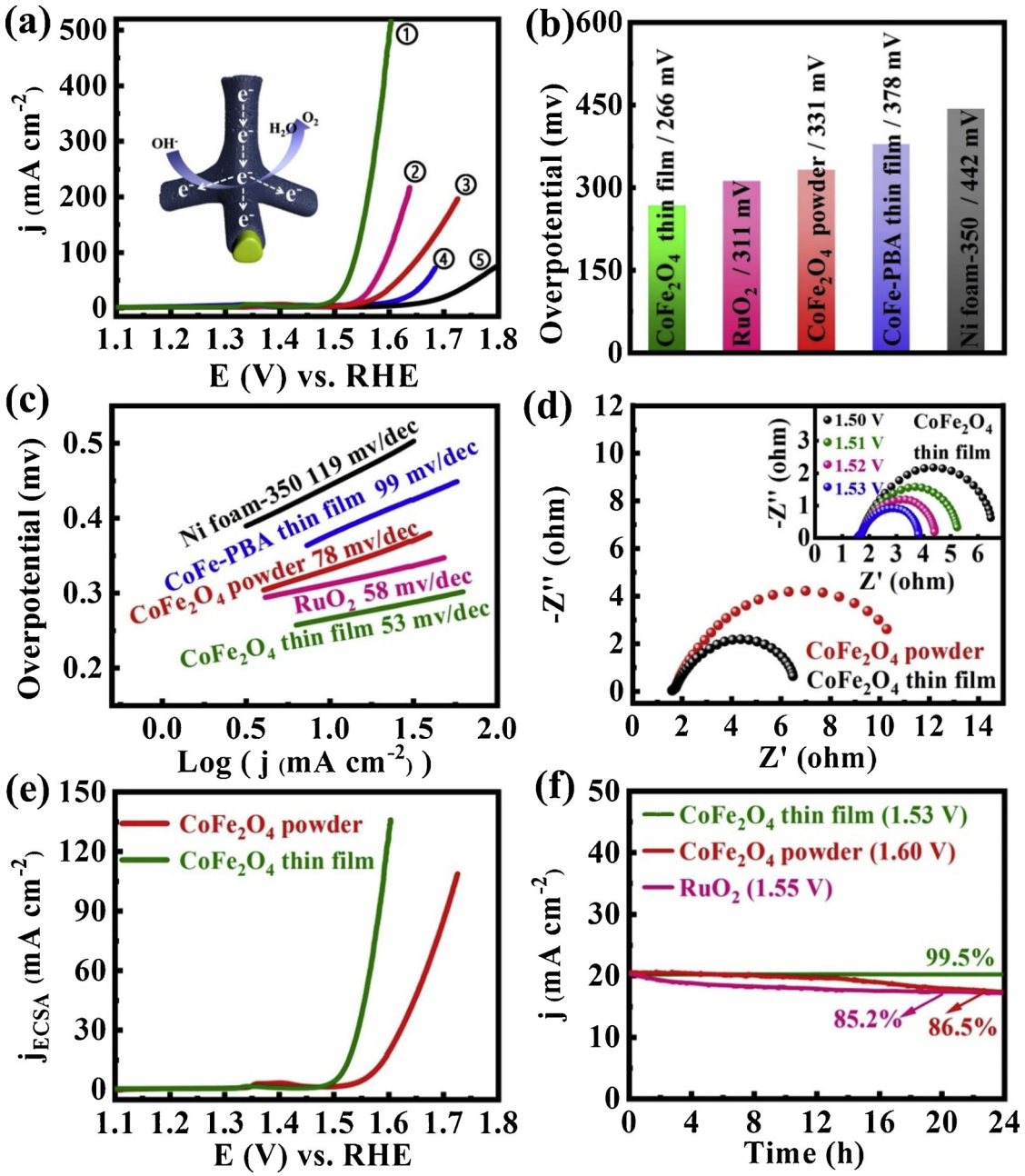

Fig. 4. (a) LSV curves (iR-corrected) of ①$CoFe_2O_4$ thin film, ②RuO_2, ③$CoFe_2O_4$ powder, ④CoFe-PBA thin film, and ⑤Ni foam-350 with a scan rate of 2 mV s^{-1}; (b) The required overpotential to offer a current density of 10 mA cm^{-2} for different electrocatalysts; (c) The corresponding Tafel plots; (d) EIS spectrum of $CoFe_2O_4$ thin film and $CoFe_2O_4$ powder recorded at 1.5 V versus RHE (inset is EIS of $CoFe_2O_4$ thin film recorded at different potentials); (e) LSV curves normalized by the ECSA; (f) Chronoamperometric curves without iR-corrected of $CoFe_2O_4$ thin film, $CoFe_2O_4$ powder, and RuO_2. All experiments were carried out in 1 M KOH.

in Figure S16, the $CoFe_2O_4$ thin film after continuous operation for 90 h at a current density of ~100 mA cm^{-2} still maintained 82.0% current density. And the $CoFe_2O_4$ thin film after working for 35 h at a current density of ~350 mA cm^{-2} still kept 81.1% current density, the corresponding SEM images after the durability test exhibited that $CoFe_2O_4$ thin film was still anchored on the surface of Ni foam with many cracks caused by the release of oxygen bubbles (Figure S17). The XPS result of Fe 2p after OER was almost identical to that of the fresh $CoFe_2O_4$ thin film. For the Co 2p XPS spectrum after OER, Co $2p_{1/2}$ peak and Co $2p_{3/2}$ peak shifted slightly to lower binding energy, indicated only a small amount of oxidation of Co(II) to Co(III) (Figure S18). This long-lasting stability at high current densities facilitates the practical application of catalysts in energy and conversion devices like fuel cells, metal–air batteries, and water electrolysers.

3.3. DFT calculations

DFT calculations have been performed to investigate adsorption energies and the variation of Gibbs free energy in those elementary steps of OER reaction on $CoFe_2O_4$ models. To study the OER catalytic activities of these structures, all possible types doping structure were built, and the preferential adsorption geometries for the adsorbates on the (110) plane of $CoFe_2O_4$ were shown in Figure S19 and Figure S20. The Gibbs free energy change on Co and Fe sites in the OER process were listed in Fig. 5 Figure S21. For the model, the Gibbs free energy for the formation of O* turns out to be the highest and becomes the rate-limiting step for water oxidation reaction, which is 2.68 and 3.08 eV for Co and Fe sites. The Tafel slope of $CoFe_2O_4$ was tested to be 53 mV dec^{-1}, implying that the rate-determining reaction is the second step,

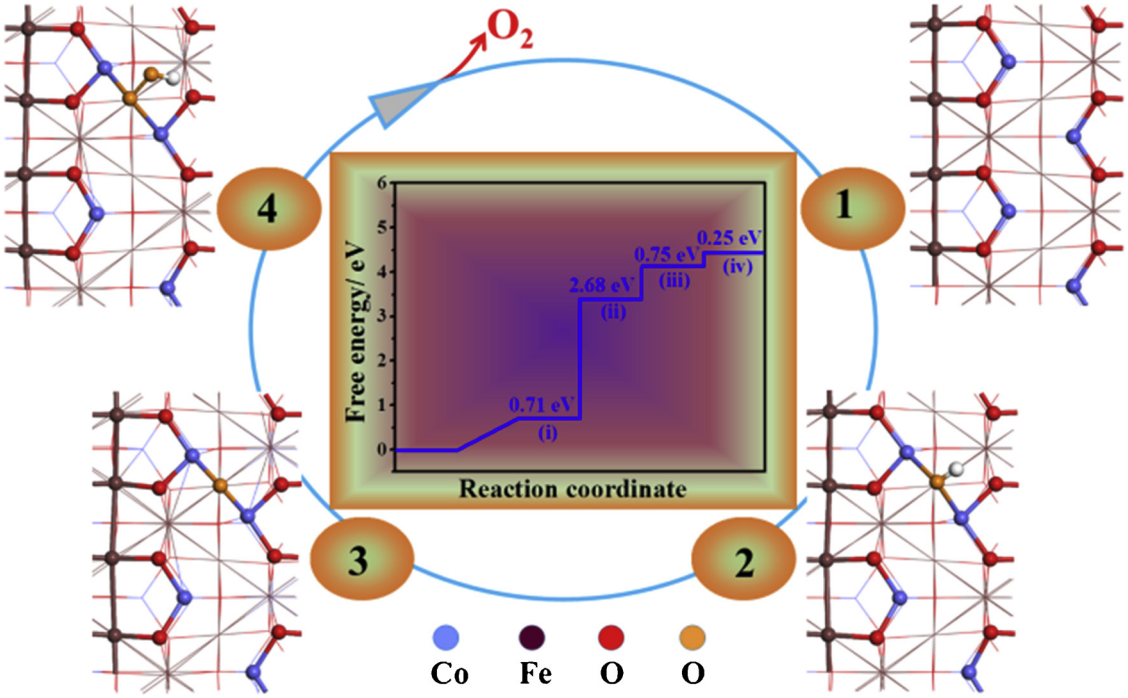

Fig. 5. The model of OER process on Co sites in the structure of $CoFe_2O_4$ with [110] orientation. The Gibbs free energy change (ΔG_i/eV, pH = 0, U = 0) of each reaction step involved in the OER process.

which is consistent with the results of theoretical calculation. The calculations in this work suggested that the overpotential value is 1.45 V, the main surface adsorbed species is OH*, and the surface Co atom is the main active site.

4. Conclusions

In summary, $CoFe_2O_4$ thin film with well-aligned spatial form is first developed from surface directly epitaxial growth of oriented CoFe-based prussian blue analogue film (CoFe-PBA thin film) for efficient and durable electrocatalytic OER. Various characterization analysis and experiments indicated that the enhanced OER performance of the $CoFe_2O_4$ thin film can be mainly attribute to the low charge transfer resistance, and the exposed abundant catalytically active sites associate with the porous structure inside the catalyst and further firmly anchored to the 3D conductive Ni foam substrate without apparent interspace. The study of present $CoFe_2O_4$ thin film derived from epitaxial growth of oriented PBA film provides an effective paradigm for preparing self-support, binder-free, high-efficiency, and durable electrocatalyst in the application of water spitting.

Acknowledgements

This work was supported by the Strategic Priority Research Program of the Chinese Academy of Sciences (XDB20000000), the National Natural Science Foundation of China (21872148, 21425102, 21601189, 21473202 and 21521061), the Youth Innovation Promotion Association of Chinese Academy of Sciences (2018339) and the Natural Science Foundation of Fujian Province (2016J01085).

Appendix A. Supplementary data

Supplementary material related to this article can be found, in the online version, at doi:https://doi.org/10.1016/j.apcatb.2018.12.036.

References

[1] Y. Zheng, Y. Jiao, Y. Zhu, L.H. Li, Y. Han, Y. Chen, M. Jaroniec, S.-Z. Qiao, High electrocatalytic hydrogen evolution activity of an anomalous ruthenium catalyst, J. Am. Chem. Soc. 138 (2016) 16174–16181.
[2] J.H. Montoya, L.C. Seitz, P. Chakthranont, A. Vojvodic, T.F. Jaramillo, J.K. Norskov, Materials for solar fuels and chemicals, Nat. Mater. 16 (2017) 70–81.
[3] X. Zhao, X. Li, Y. Yan, Y. Xing, S. Lu, L. Zhao, S. Zhou, Z. Peng, J. Zeng, Electrical and structural engineering of cobalt selenide nanosheets by Mn modulation for efficient oxygen evolution, Appl. Catal. B: Environ. 236 (2018) 569–575.
[4] G. Liu, P. Li, G. Zhao, X. Wang, J. Kong, H. Liu, H. Zhang, K. Chang, X. Meng, T. Kako, J. Ye, Promoting active species generation by plasmon-induced hot-electron excitation for efficient electrocatalytic oxygen evolution, J. Am. Chem. Soc. 138 (2016) 9128–9136.
[5] C. Walter, P.W. Menezes, S. Orthmann, J. Schuch, P. Connor, B. Kaiser, M. Lerch, M. Driess, A molecular approach to manganese nitride acting as a high performance electrocatalyst in the oxygen evolution reaction, Angew. Chem. Int. Ed. 57 (2018) 698–702.
[6] K. Mamtani, D. Jain, D. Dogu, V. Gustin, S. Gunduz, A.C. Co, U.S. Ozkan, Insights into oxygen reduction reaction (ORR) and oxygen evolution reaction (OER) active sites for nitrogen-doped carbon nanostructures (CN_x) in acidic media, Appl. Catal. B: Environ. 220 (2018) 88–97.
[7] M. Kim, S. Kim, D. Song, S. Oh, K.J. Chang, E. Cho, Promotion of electrochemical oxygen evolution reaction by chemical coupling of cobalt to molybdenum carbide, Appl. Catal. B: Environ. 227 (2018) 340–348.
[8] J. Masa, P. Weide, D. Peeters, I. Sinev, W. Xia, Z. Sun, C. Somsen, M. Muhler, W. Schuhmann, Amorphous cobalt boride (Co_2B) as a highly efficient nonprecious catalyst for electrochemical water splitting: oxygen and hydrogen evolution, Adv. Energy Mater. 6 (2016) 2502313.
[9] M. Li, Y. Xiong, X. Liu, X. Bo, Y. Zhang, C. Han, L. Guo, Facile synthesis of electrospun MFe_2O_4 (M = Co, Ni, Cu, Mn) spinel nanofibers with excellent electrocatalytic properties for oxygen evolution and hydrogen peroxide reduction, Nanoscale 7 (2015) 8920–8930.
[10] Y. Liu, J. Li, F. Li, W. Li, H. Yang, X. Zhang, Y. Liu, J. Ma, A facile preparation of $CoFe_2O_4$ nanoparticles on polyaniline-functionalised carbon nanotubes as enhanced catalysts for the oxygen evolution reaction, J. Mater. Chem. A Mater. Energy Sustain. 4 (2016) 4472–4478.
[11] Q. Zhao, Z. Yan, C. Chen, J. Chen, Spinels: controlled preparation, oxygen Reduction/Evolution reaction application, and beyond, Chem. Rev. 117 (2017) 10121–10211.
[12] H. Zhu, S. Zhang, Y.-X. Huang, L. Wu, S. Sun, Monodisperse $M_xFe_{3-x}O_4$ (M = Fe, Cu, Co, Mn) nanoparticles and their electrocatalysis for oxygen reduction reaction, Nano Lett. 13 (2013) 2947–2951.
[13] B. Cui, H. Lin, J.-B. Li, X. Li, J. Yang, J. Tao, Core-ring structured $NiCo_2O_4$ nanoplatelets: synthesis, characterization, and electrocatalytic applications, Adv. Funct. Mater. 18 (2008) 1440–1447.
[14] B. Kong, C. Selomulya, G. Zheng, D. Zhao, New faces of porous Prussian blue: interfacial assembly of integrated hetero-structures for sensing applications, Chem.

Soc. Rev. 44 (2015) 7997–8018.
[15] C.H. Li, M.K. Peprah, D. Asakura, M.W. Meisel, M. Okubo, D.R. Talham, Stepwise reduction of electrochemically lithiated core-shell heterostructures based on the prussian blue analogue coordination polymers $K_{0.1}Cu[Fe(CN)_6]_{0.7}\cdot 3.5H_2O$ and $K_{0.1}Ni\ [Fe(CN)_6]_{0.7}\cdot 4.4H_2O$, Chem. Mater. 27 (2015) 1524–1530.
[16] Y. Huang, M. Xie, J. Zhang, Z. Wang, Y. Jiang, G. Xiao, S. Li, L. Li, F. Wu, R. Chen, A novel border-rich Prussian blue synthetized by inhibitor control as cathode for sodium ion batteries, Nano Energy 39 (2017) 273–283.
[17] H. Guo, T. Li, W. Chen, L. Liu, X. Yang, Y. Wang, Y. Guo, General design of hollow porous $CoFe_2O_4$ nanocubes from metal-organic frameworks with extraordinary lithium storage, Nanoscale 6 (2014) 15168–15174.
[18] X.-Y. Yu, L. Yu, H.B. Wu, X.W. Lou, Formation of nickel sulfide nanoframes from metal-organic frameworks with enhanced pseudocapacitive and electrocatalytic properties, Angew. Chem. Int. Ed. 54 (2015) 5331–5335.
[19] A.K. Das, R. Bera, A. Maitra, S.K. Karan, S. Paria, L. Halder, S.K. Si, A. Bera, B.B. Khatua, Fabrication of an advanced asymmetric supercapacitor based on a microcubical PB@MnO_2 hybrid and PANI/GNP composite with excellent electrochemical behaviour, J. Mater. Chem. A Mater. Energy Sustain. 5 (2017) 22242–22254.
[20] S. Pintado, S. Goberna-Ferron, E.C. Escudero-Adan, J. Ramon Galan-Mascaros, Fast and persistent electrocatalytic water oxidation by Co-Fe prussian blue coordination polymers, J. Am. Chem. Soc. 135 (2013) 13270–13273.
[21] L. Han, P. Tang, A. Reyes-Carmona, B. Rodriguez-Garcia, M. Torrens, J. Ramon Morante, J. Arbiol, J. Ramon Galan-Mascaros, Enhanced activity and acid pH stability of prussian blue-type oxygen evolution electrocatalysts processed by chemical etching, J. Am. Chem. Soc. 138 (2016) 16037–16045.
[22] X. Wang, L. Yu, B.Y. Guan, S. Song, X.W. Lou, Metal-organic framework hybrid-assisted formation of Co_3O_4/Co-Fe oxide double-shelled nanoboxes for enhanced oxygen evolution, Adv. Mater. 30 (2018) 1801211.
[23] L. Han, X.-Y. Yu, X.W. Lou, Formation of prussian-blue-Analog nanocages via a direct etching method and their conversion into Ni-Co-Mixed oxide for enhanced oxygen evolution, Adv. Mater. 28 (2016) 4601–4605.
[24] M.B. Stevens, L.J. Enman, A.S. Batchellor, M.R. Cosby, A.E. Vise, C.D.M. Trang, S.W. Boettcher, Measurement techniques for the study of thin film heterogeneous water oxidation electrocatalysts, Chem. Mater. 29 (2017) 120–140.
[25] G. Jia, W. Zhang, G. Fan, Z. Li, D. Fu, W. Hao, C. Yuan, Z. Zou, Three-dimensional hierarchical architectures derived from surface-mounted metal-organic framework membranes for enhanced electrocatalysis, Angew. Chem. Int. Ed. 56 (2017) 13781–13785.
[26] I.S. Amiinu, X. Liu, Z. Pu, W. Li, Q. Li, J. Zhang, H. Tang, H. Zhang, S. Mu, From 3D ZIF nanocrystals to Co-N_x/C nanorod array electrocatalysts for ORR, OER, and Zn-Air batteries, Adv. Funct. Mater. 28 (2018) 1704638.
[27] T. Tang, W.-J. Jiang, S. Niu, N. Liu, H. Luo, Q. Zhang, W. Wen, Y.-Y. Chen, L.-B. Huang, F. Gao, J.-S. Hu, Kinetically controlled coprecipitation for general fast synthesis of sandwiched metal hydroxide nanosheets/graphene composites toward efficient water splitting, Adv. Funct. Mater. 28 (2018) 1704594.
[28] M. Hu, S. Ishihara, K. Ariga, M. Imura, Y. Yamauchi, Kinetically controlled crystallization for synthesis of monodispersed coordination polymer nanocubes and their self-assembly to periodic arrangements, Chem.-Eur. J. 19 (2013) 1882–1885.
[29] T. Uemura, S. Kitagawa, Prussian blue nanoparticles protected by poly(vinylpyrrolidone), J. Am. Chem. Soc. 125 (2003) 7814–7815.
[30] R.A. Fischer, C. Woell, Layer-by-Layer liquid-phase epitaxy of crystalline coordination polymers at surfaces, Angew. Chem. Int. Ed. 48 (2009) 6205–6208.
[31] O. Shekhah, M. Eddaoudi, The liquid phase epitaxy method for the construction of oriented ZIF-8 thin films with controlled growth on functionalized surfaces, Chem. Commun. (Camb.) 49 (2013) 10079–10081.
[32] B. Liu, M. Tu, D. Zacher, R.A. Fischer, Multi variant surface mounted metal-organic frameworks, Adv. Funct. Mater. 23 (2013) 3790–3798.
[33] D.-J. Li, Z.-G. Gu, I. Vohra, Y. Kang, Y.-S. Zhu, J. Zhang, Epitaxial growth of oriented metalloporphyrin network thin film for improved selectivity of volatile organic compounds, Small 13 (2017) 1604035.
[34] D.-J. Li, Z.-G. Gu, W. Zhang, Y. Kang, J. Zhang, Epitaxial encapsulation of homodispersed CeO_2 in a cobalt-porphyrin network derived thin film for the highly efficient oxygen evolution reaction, J. Mater. Chem. A Mater. Energy Sustain. 5 (2017) 20126–20130.
[35] M.I. Vohra, D.-J. Li, Z.-G. Gu, J. Zhang, Insight into the epitaxial encapsulation of Pd catalysts in an oriented metalloporphyrin network thin film for tandem catalysis, Nanoscale 9 (2017) 7734–7738.
[36] M. Tsotsalas, J. Liu, B. Tettmann, S. Grosjean, A. Shahnas, Z. Wang, C. Azucena, M. Addicoat, T. Heine, J. Lahann, J. Overhage, S. Braese, H. Gliemann, C. Woell, Fabrication of highly uniform gel coatings by the conversion of surface-anchored metal-organic frameworks, J. Am. Chem. Soc. 136 (2014) 8–11.
[37] Z.-G. Gu, S.-C. Chen, W.-Q. Fu, Q. Zheng, J. Zhang, Epitaxial growth of MOF thin film for modifying the dielectric layer in organic field-effect transistors, ACS appl, Mater. Interfaces 9 (2017) 7259–7264.
[38] A.A. Talin, A. Centrone, A.C. Ford, M.E. Foster, V. Stavila, P. Haney, R.A. Kinney, V. Szalai, F. El Gabaly, H.P. Yoon, F. Leonard, M.D. Allendorf, Tunable electrical conductivity in metal-organic framework thin-film devices, Science 343 (2014) 66–69.
[39] O. Shekhah, J. Liu, R.A. Fischer, C. Woell, MOF thin films: existing and future applications, Chem. Soc. Rev. 40 (2011) 1081–1106.
[40] J. Liu, C. Woell, Surface-supported metal-organic framework thin films: fabrication methods, applications, and challenges, Chem. Soc. Rev. 46 (2017) 5730–5770.
[41] J.P. Perdew, K. Burke, M. Ernzerhof, Generalized gradient approximation made simple, Phys. Rev. Lett. 77 (1996) 3865–3868.
[42] J.K. Norskov, J. Rossmeisl, A. Logadottir, L. Lindqvist, J.R. Kitchin, T. Bligaard, H. Jonsson, Origin of the overpotential for oxygen reduction at a fuel-cell cathode, J. Phys. Chem. B 108 (2004) 17886–17892.
[43] J. Rossmeisl, Z.W. Qu, H. Zhu, G.J. Kroes, J.K. Norskov, Electrolysis of water on oxide surfaces, J. Electroanal. Chem. Lausanne (Lausanne) 607 (2007) 83–89.
[44] A. Valdes, Z.W. Qu, G.J. Kroes, J. Rossmeisl, J.K. Norskov, Oxidation and photo-oxidation of water on TiO_2 surface, J. Phys. Chem. C 112 (2008) 9872–9879.
[45] Z. Zhuo, X. Wu, J. Yang, Two-dimensional phosphorus porous polymorphs with tunable band gaps, J. Am. Chem. Soc. 138 (2016) 7091–7098.
[46] X. Li, P. Cui, W. Zhong, J. Li, X. Wang, Z. Wang, J. Jiang, Graphitic carbon nitride supported single-atom catalysts for efficient oxygen evolution reaction, Chem. Commun. (Camb.) 52 (2016) 13233–13236.
[47] J. Wirth, R. Neumann, M. Antonietti, P. Saalfrank, Adsorption and photocatalytic splitting of water on graphitic carbon nitride: a combined first principles and semiempirical study, Phys. Chem. Chem. Phys. 16 (2014) 15917–15926.
[48] B.K. Kang, M.H. Woo, J. Lee, Y.H. Song, Z. Wang, Y. Guo, Y. Yamauchi, J.H. Kim, B. Lim, H. Yoon, Mesoporous Ni-Fe oxide multi-composite hollow nanocages for efficient electrocatalytic water oxidation reactions, J. Mater. Chem. A Mater. Energy Sustain. 5 (2017) 4320–4324.
[49] X. Li, L. Yuan, J. Wang, L. Jiang, A.I. Rykov, D.L. Nagy, C. Bogdan, M.A. Ahmed, K. Zhu, G. Sun, W. Yang, A "copolymer-co-morphology" conception for shape-controlled synthesis of Prussian blue analogues and as-derived spinel oxides, Nanoscale 8 (2016) 2333–2342.
[50] W. Wan, X. Liu, H. Li, X. Peng, D. Xi, J. Luo, 3D carbon framework-supported CoNi nanoparticles as bifunctional oxygen electrocatalyst for rechargeable Zn-air batteries, Appl. Catal. B 240 (2019) 193–200.
[51] C.A. Chagas, E.F. de Souza, M.C.N.A. de Carvalho, R.L. Martins, M. Schmal, Cobalt ferrite nanoparticles for the preferential oxidation of CO, Appl. Catal. A Gen. 519 (2016) 139–145.
[52] Y. Li, C. Zhao, Enhancing water oxidation catalysis on a synergistic phosphorylated NiFe hydroxide by adjusting catalyst wettability, ACS Catal. 7 (2017) 2535–2541.
[53] F. Zheng, D. Zhu, X. Shi, Q. Chen, Metal-organic framework-derived porous $Mn_{1.8}Fe_{1.2}O_4$ nanocubes with an interconnected channel structure as high-performance anodes for lithium ion batteries, J. Mater. Chem. A Mater. Energy Sustain. 3 (2015) 2815–2824.
[54] C. Guan, X. Liu, W. Ren, X. Li, C. Cheng, J. Wang, Rational design of metal-organic framework derived hollow $NiCo_2O_4$ arrays for flexible supercapacitor and electrocatalysis, Adv. Energy Mater. 7 (2017) 1602391.
[55] Y. Feng, J. Wei, Y. Ding, Efficient Photochemical, Thermal, and electrochemical water oxidation catalyzed by a porous iron-based oxide derived metal organic framework, J. Phys. Chem. C 120 (2016) 517–526.
[56] B. Kang, X. Jin, S.M. Oh, S.B. Patil, M.G. Kim, S.H. Kim, S.-J. Hwang, An effective way to improve bifunctional electrocatalyst activity of manganese oxide via control of bond competition, Appl. Catal. B: Environ. 236 (2018) 107–116.
[57] C.C.L. McCrory, S. Jung, I.M. Ferrer, S.M. Chatman, J.C. Peters, T.F. Jaramillo, Benchmarking hydrogen evolving reaction and oxygen evolving reaction electrocatalysts for solar water splitting devices, J. Am. Chem. Soc. 137 (2015) 4347–4357.
[58] H. Liang, A.N. Gandi, D.H. Anjum, X. Wang, U. Schwingenschlogl, H.N. Alshareef, Plasma-assisted synthesis of NiCoP for efficient overall water splitting, Nano Lett. 16 (2016) 7718–7725.
[59] J. Zhou, Y. Dou, A. Zhou, R.-M. Guo, M.-J. Zhao, J.-R. Li, MOF template-directed fabrication of hierarchically structured electrocatalysts for efficient oxygen evolution reaction, Adv. Energy Mater. 7 (2017) 602643.